Batteries & Supercaps

Research Article
doi.org/10.1002/batt.202200100

Chemistry Europe
European Chemical
Societies Publishing

www.batteries-supercaps.org

Surface Functionalization of LiNi$_{7.0}$Co$_{0.15}$Mn$_{0.15}$O$_2$ with Fumed Li$_2$ZrO$_3$ via a Cost-Effective Dry-Coating Process for Enhanced Performance in Solid-State Batteries

Sahin Cangaz,[a, b] Felix Hippauf,[b] Ryo Takata,[c] Franz Schmidt,[c] Susanne Dörfler,[b] and Stefan Kaskel*[a, b]

Applying a thin film coating is a vital strategy to enhance long term and interface stability of Ni-rich layered oxide cathode materials (NRLOs), especially when they are matched with sulfidic solid electrolytes (SSEs) in solid-state batteries (SSBs). The coating prevents direct contact between the cathode active material (CAM) and the SSE, shielding against parasitic side reactions at the cathode electrolyte interface (CEI). Conventional coatings are based on wet-chemical methods and therefore harmful to the environment and require long-lasting processing and high costs. In this study, we present a versatile, facile and highly-scalable dry-coating method (with suitable equipment up to 500 kg per batch) successfully employed for both *multi*-

and *single*-crystalline LiNi$_{0.70}$Mn$_{0.15}$Co$_{0.15}$O$_2$ (NCM70) particles by fumed Li$_2$ZrO$_3$ nanostructured particles (LZONPs) via high intensity mixing process. The resulting porous coating layer stays firmly attached at the CAM particle surface without a need of *post*-calcination step at elevated temperatures. The electrochemical testing results signify enhanced rate capability up to 1.5 mA cm^{-2} for both particle types and cyclic stability up to 650 cycles with a capacity retention of 86.1% for *single*-crystalline NCM70. We attribute the enhanced performance to the reduced CEI reactions as cathodic charge transfer resistance depressed significantly after dry-coating by LZONPs, being an important step towards sulfidic solid-state batteries.

Introduction

In recent years, the research efforts on solid-state batteries (SSBs) have intensified tremendously as they offer higher safety and energy density, when compared to liquid electrolyte-based lithium ion batteries (LIBs). Both criteria are crucial for application of stationary energy systems and electric vehicles (EVs) without any concerns about range (at least ≥ 500 km per charge)[1–3] and safety.[4] In this context, non-flammable solid electrolytes (SEs) appear as alternatives that can eliminate the security risks originating from liquid electrolytes utilized in state-of-art LIBs – more specifically, leakage and ignition of electrolytes. Beside the safety problems, electrode materials used in traditional LIBs, i.e., LiCoO$_2$ (LCO, 140 mAh g^{-1}) and

graphite (370 mAh g^{-1}), do not compensate growing energy demands for electric devices any more due to their restricted specific energies.[5,6] Hence, combining SEs with high energy electrodes (HEEs), for instance, metallic lithium (2870 mAh g^{-1}),[7–10] silicon anodes (3579 mAh g^{-1}),[11–14] "so-called" Li-free anode approaches[15–17] and Ni-Rich layered oxide cathodes (NRLOs), i.e., LiNi$_x$Co$_y$Mn$_{1-x-y}$O$_2$, $x \geq 5$, NCM (170–220 mAh g^{-1}),[18–20] is seen as a common strategy to simultaneously overcome with safety and energy density issues.

Accordingly, several research groups[21–26] have put extreme effort to develop such a solid electrolyte that exhibits competitive ionic conductivity (≥ 10 mS cm^{-1} at 25 °C), formability and interface stability against HEEs to outperform liquid electrolytes in the matter of cell performance and energy densities (≥ 750 Wh L^{-1} or 350 Wh kg^{-1})[27] Amongst SEs, sulfidic solid electrolytes (SSEs) are drawing much attraction because of their high ionic conductivity (≥ 2 mS cm^{-1} at 25 °C)[28,29] and moderate ductility (E-moduli: 20 GPa),[30] making them favorable in terms of cell kinetics and processability. Meanwhile, NRLOs become more prominent as compared to high voltage cathodes i.e., LiMn$_2$O$_4$ and are more frequently employed in SSBs using SSE due to their higher specific capacity.[31]

Nevertheless, the aforementioned advantages of SSEs and NRLOs are not solely sufficient to accomplish safe batteries with high energy/power density. More importantly, electrochemical compatibility between SSE, cathode and anode must be considered. In particular, excellent interface stability between SSE and cathode material is extremely required since the highest portion of overall cell resistance emerges from

[a] S. Cangaz, Prof. Dr. S. Kaskel
     Department of Inorganic Chemistry I
     Technische Universität Dresden
     Bergstraße 66, 01069 Dresden, Germany
     E-mail: stefan.kaskel@tu-dresden.de
[b] S. Cangaz, Dr. F. Hippauf, Dr. S. Dörfler, Prof. Dr. S. Kaskel
     Business Unit Chemical Surface Technology
     Fraunhofer Institute for Material and Beam Technology (IWS)
     Winterbergstraße 28, 01277 Dresden, Germany
[c] R. Takata, F. Schmidt
     Research Development & Innovation
     Evonik Operations GmbH
     Rodenbacher Chaussee 4, Hanau-Wolfgang 63457, Germany

Batteries & Supercaps

Research Article
doi.org/10.1002/batt.202200100

Chemistry Europe
European Chemical
Societies Publishing

interfacial impedance at the cathode electrolyte interface (CEI), limiting rate performance and cycling life of SSBs.[32]

Until today, apart from many others, two major reasons have been explored accounting for huge CEI resistance in SSBs; 1) mechanical disintegration of CEI layer/poor interparticle contact due to contraction/expansion of NRLOs particles ($\pm 7\%$) during cycling[33,34] and 2) formation of highly impeding side reaction products such as LiCl, S and SO_3^{2-}.[35,36]

To minimize CEI resistance, applying a thin surface coating (2–10 nm) in low mass fraction (0.5–2 wt%) of electrochemically inactive materials to NRLOs particles is a key approach as it acts as buffer layer suppressing parasitic side reactions. For that purpose, various metal oxides have been successfully employed for NRLOs such as Li_2TiO_3 (LTO),[37–39] $LiNbO_3$ (LNO),[40,41] Li_2ZrO_3 (LZO)[42,43] and $LiAlO_2$ (LAO),[44] resulting in reduction of CEI resistance. However, most of these coatings are carried out by wet chemical methods such as sol-gel[45,46] and solution-based process.[47] These coating procedures are unfavorable as they involve the usage of expensive precursors and highly volatile organic components (VOCs), resulting in high costs and the release of harmful gases into the atmosphere. Moreover, sol-gel coatings often require *post*-annealing steps at elevated temperatures ($\geq 900\,°C$),[48,49] which further increase production costs. Alternatively, solvent-free approaches, i.e., dry-coating of CAM particles, have recently drawn significant attention. In this technique, coating precursors or/and nanoparticles are simply mixed with CAM particles. An intimate contact between coating and host particles is readily formed due to strong van der Waals interactions and applied high mechanical forces during this procedure.[50] Promising results have already been reported for NRLOs via simply mixing by boric acid,[51] Al_2O_3 nanostructured particles[50] and LNO nanoparticles.[40] However, only few publications have addressed utilization of dry-coated NRLOs for SSBs so far.

This work presents a facile and versatile solvent-free dry-coating process (Figure 1), which was successfully applied for both *single*-crystalline (sc) and *multi*-crystalline (mc) NCM70 granules (particle size: 4–5 μm and 8–10 μm, respectively). Fumed metal oxide nanostructured particles (particle size, 20–200 nm) were implemented as coating layer with various coating dosages (1–2 wt%). The coating was performed by use of a scalable high energy mixing process, an environmentally friendly and cost-effective technique. The resulting coating layers exhibit a homogeneous and conformal distribution of fumed oxide nanostructured particles at the NCM70 surface regardless of particle type as shown by morphological characterization.

In the following we demonstrate how the dry-coating procedure enhances the electrochemical performance of resulting CAM, 1LZO-NCM70. The performance of the CAM, which was investigated in SSB cell configuration using SSE Li_6PS_5Cl and Li−In as anode, exhibits improved rate (up to 1.5 mA cm^{-2}) capability and long-term cycling stability (≥ 650 cycles) for areal capacities of 1.5 mAh cm^{-2} in case of *sc* particle type even without further heat treatment of the coating. This new dry process significantly reduces energy consumption and emission of organic solvents while facilitating a protective coating technology for active material particles to potentially produce long-term SSB prototype cells.

Results and Discussion

Structural characterization of LZONPs

LZONPs that were used as coating material were prepared by flame-spray pyrolysis (FSP). XRD diffractogram (Figure 2a) shows that the coating material exhibits two LZO phases with tetragonal structure, namely t-Li_2ZrO_3 (PDF#00-020-0647) and
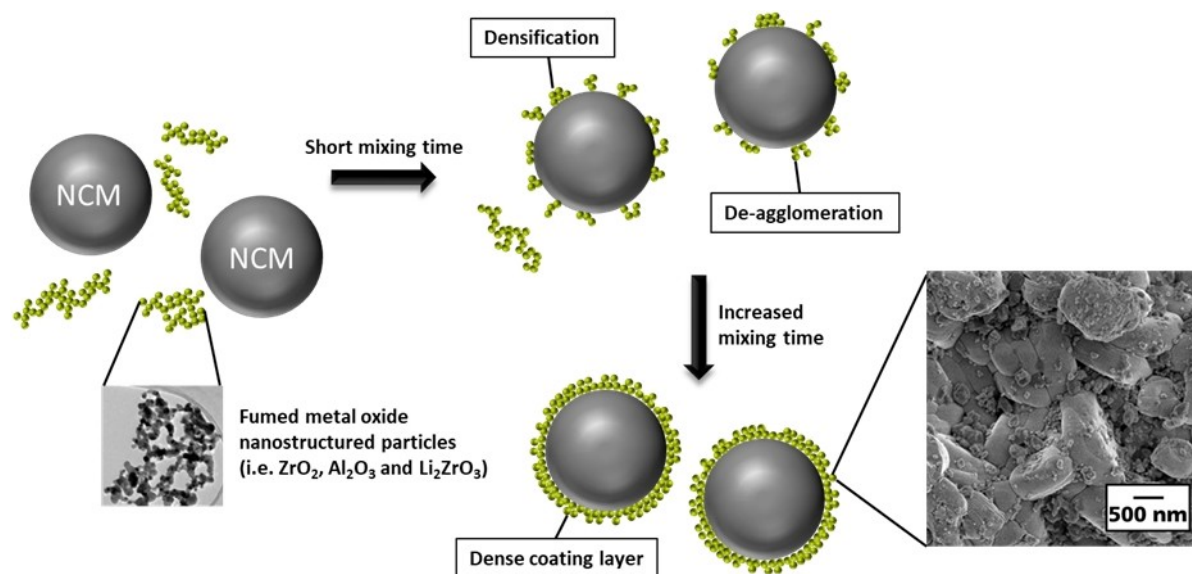

Figure 1. Schematic illustration of the dry-coating procedure of NRLO particles by fumed metal oxide agglomerates.
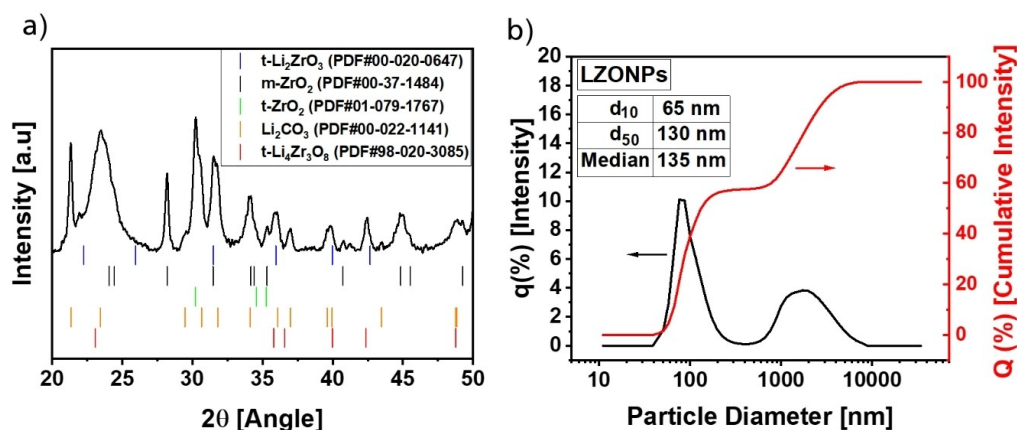
Figure 2. a) XRD pattern and b) particle size distribution of LZONPs represented by intensity (*q*%, black line) and cumulative intensity (red line) for nanostructured particles produced via flame spray pyrolysis.

t-$Li_4Zr_3O_8$ (PDF#98-020-3085). The strong reflections at around 21.3° and 23.5° together with the peaks located between 27.9° and 36.6° refer to the presence of Li_2CO_3 (PDF#00-022-1141) and ZrO_2 (PDF#01-079-1767), respectively. A *post*-annealing step is often required at elevated temperatures (650 °C) for prolonged time (4–5 h) in order to obtain LZO with high degree of crystallinity out of Li_2CO_3 and ZrO_2 (Figure S5). The dominance of these two precursor phases in the coating material implies that LZO crystallizes partially and might be present in amorphous phase as well. Notably, the low degree of crystallinity of the LZO coating (amorphous phase) is beneficial for Li^+ ion transport kinetics at the CEI, as the lattice mismatch between highly-crystalline LZO and NCM70 can hinder ionic pathways.[52]

The cumulative intensity in the particle size distribution (PSD) for LZONPs (Figure 2b), designates that 50 % of counted particles are small aggregates having a particle size $\leq$ 130 nm (d_{50}). Furthermore, some particles with a size above 1000 nm are also observable, indicating the presence of larger LZO agglomerates.

HR-TEM images of LZONPs (Figure 6a–c) agrees with the above XRD and PSD analyses. For the first, no well-defined crystal planes are observable, when looking at the individual particles, signifying relatively amorphous phase. For the second, the coating material consists of primary particles (10–20 nm) that branch into LZO aggregates (130–150 nm). These constituent nanostructured particles form strong chemical bond with each other in the flame over the course of spray pyrolysis and cannot be easily defragmented via high intensity mixing process.[53] On the other hand, their high specific surface area of 25 $m^2 g^{-1}$ is especially beneficial for the following coating process and leads to a strong interaction with the CAM. Note that a thin surface layer with the thickness of ~2.5 nm (Figure 3c) on individual nanostructured particles is also visible. This layer can be attributed to Li_2CO_3 since constituent Li precursor in the flame is in gaseous phase during FSP and condenses as Li_2CO_3 on readily-formed solid LZONPs as the flame temperature decreases.[54]
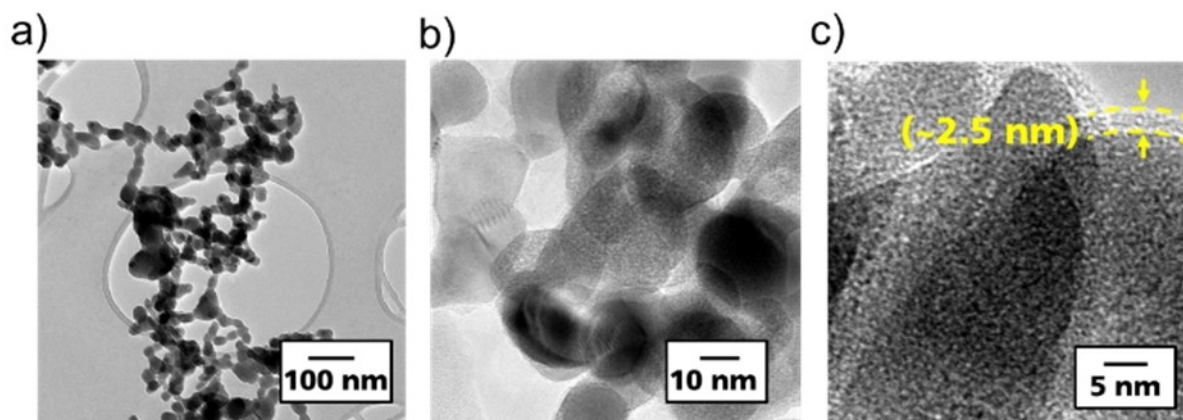

Figure 3. A HR-TEM image of fumed LZO nanostructured particles with the magnification of a) 25000×, b) 250000× and c) 600000×.

Batteries & Supercaps

Research Article
doi.org/10.1002/batt.202200100

Chemistry Europe
European Chemical
Societies Publishing

Structural characterization of multi-crystalline NCM70 particles coated by LZONPs

XRD patterns (Figure 4a) confirm high degree of crystallinity for *mc*-pristine (pristine_mc) and 1 wt% dry-coated NCM70 by LZONPs (1LZO-NCM70_mc) materials since their respective peaks match with the given reference values for hexagonal α-NaFeO$_2$ crystal structure with $R\bar{3}m$ space group.[55] Also, the absence of any additional peaks in two XRD patterns signifies impurity-free pristine and LZO coated NCM70. Notably, no peaks of the coating material are visible in XRD pattern of 1LZO-NCM70_mc, as the low mass fraction of LZO is beyond the detection limits of our XRD instrument. Moreover, LZO dry-coating does not damage NCM70 crystal structure since (108)/(110) diffraction peaks appear to be split. Furthermore, the main (104) reflection (Figure 4b) is identical, indicating a preserved layered structure as well as no zirconium ion incorporation into the lattice of NCM70 after LZO coating after LZO coating.[37] The SEM image (Figure 5a) resolves that the particle size of the LZO coated NCM70 is around 8–10 μm. EDX mappings (Figure 5b and c) confirms the formation of LZO as surface layer on NCM70 since Zr atoms homogenously distributed over the surface of particles. Besides, some blue points are visible in Zr signal that are attributed to LZO agglomerates ≥ 1000 nm (Figure 2b) being in good accordance with previous PSD results of LZONPs.

Interestingly, the HR-SEM images of a single 1LZO-NCM70_mc particle (Figure 6a–c) display that fumed LZONPs fill the cavities between primary submicron particles at the surface, smoothening the rough surface of the *mc*-NCM70 granules after LZO coating (Figure S6). Notably, the resulting particle coating at CAM is not completely dense.
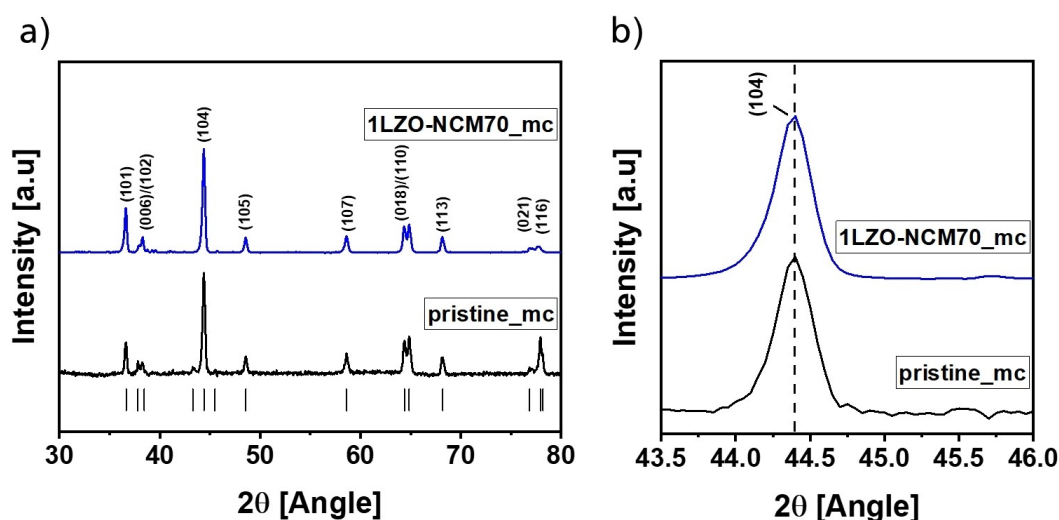

Figure 4. a) XRD patterns for pristine (black) and 1 wt% LZO coated NCM70 (blue), and b) their magnified main XRD reflection (104).
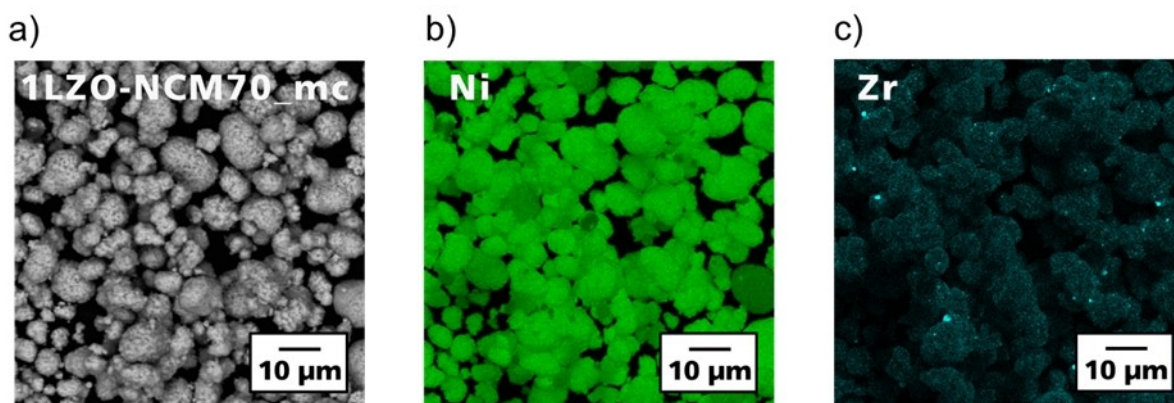

Figure 5. SEM Image of a) pristine and b) 1 wt% LZO coated NCM70 and c) respective EDX mapping of (b) acquired for Zr atoms.
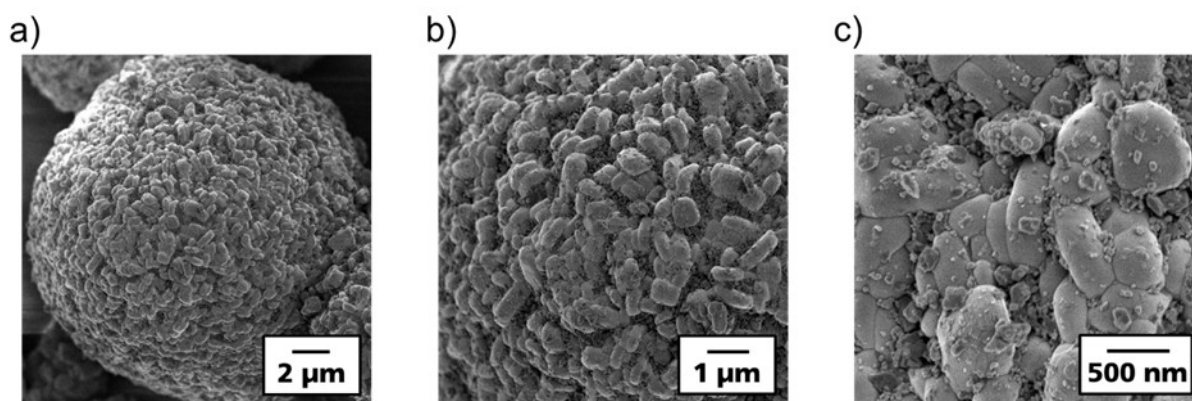
Batteries & Supercaps

Research Article
doi.org/10.1002/batt.202200100

Chemistry Europe
European Chemical
Societies Publishing

Figure 6. HR-SEM images of a single 1LZO-NCM70 particle, acquired with the magnification of a) 4500×, b) 10000× and c) 30000×.

Electrochemical characterization of multi-crystalline NCM70 particles dry-coated by LZONPs

We note that LZO (VP LZO, Evonik Operations GmbH) is found to be best performing material out of other coatings such as Al_2O_3 and ZrO_2 (Figure S7) as it exhibits high Li^+ ion conductivity and good electrochemical stability.[56] Besides, the optimum coating dosage is 1 wt% since it provides a moderate coating thickness that does not impede electron transport at the CEI,[42] leading to the best electrochemical rate performance as compared to 2 wt% (Figure S8). Furthermore, a *post*-calcination step at elevated temperatures (350 °C or 650 °C) is not required for 1 wt%. High mechanical forces applied during the process provide already an intimate contact between CAM and the coating material due to the high specific surface area of guest nanoparticles.[57,58] The annealing-step is only beneficial in case of 2 wt% LZO coating, as it condenses the thick coating layer into a thinner film, ensuring better electronic transport through the interface, enhancing rate capability (Figure S9). Bear in mind that the effect of coating dosage and annealing step on the crystal structure and particle morphology of NCM70 is negligible (Figure S10). Nevertheless 2 wt% LZO coated NCM70 calcined at 650 °C still cannot outperform the 1 wt% LZO coated NCM70 without calcination step. Therefore, we focus on only pristine and 1 wt% LZO coated materials as next, which are labelled as given in the Table 1.

To analyze the performance of the pristine and LZO coated active materials, the test cells were built and subjected to electrochemical testing. Since the study was focused on the influence of LZO coating on the cathode material in this study, we avoided using Li metal as counter electrode, as it causes severe instabilities like dendrite growth, short-circuits and chemo-mechanical failures.[36,59] Instead, Li–In anode was chosen as counter electrode as it shows a stable potential (0.62 V vs. Li), excluding the altering cathode potential due to changing anode potential during the operation of cell. Moreover, as compared to Li metal, Li–In alloy reduces the possibility of short-circuiting due to dendrite growth and possesses lithium reservoir to compensate for lithium losses.

Comparing the pristine (pristine_mc) with coated material (1LZO-NCM70 mc), during first discharge of the rate performance test, the extracted capacity rises from 134 to 146 mAh g^{-1}$_{NCM}$ (Figure 7a and b). Remarkably, the discharge capacity boosts from 49 mAh g^{-1}$_{NCM}$ up to 94 mAh g^{-1}$_{NCM}$ at the highest discharge current of 1.5 mA cm^{-2} (C-rate), almost doubling the extracted capacity. Furthermore, a slight improvement from 63% to 65% is also visible in terms of initial columbic efficiency (ICE). This enhancement can be ascribed to the LZO coating and coexistence of Li_2CO_3 on the coating material which further assists the suppression of interfacial reactions by enclosing the uncoated sides of the CAM.[60] Moreover, ternary oxide coatings consisting of mixed phase structure, i.e., Li_3BO_3-Li_2CO_3,[61] $LiNbO_3$-Li_2CO_3,[62,63] were shown to enhance long term stability of NRLOs in SSBs due to more rigid coating layer, when compared to the performance of NRLOs coated with solely LBO or LNO. EIS was conducted to resolve the reason for the performance enhancement above (Figure 6c). The impedance data were recorded after first charge at 3.63 V followed by a constant voltage step To fit the impedance spectra, an equivalent circuit of R_{bulk} $(R_{gb}Q_{gb})(R_{CT,C}Q_{CT,C})(R_{CT,A}Q_{CT,A})Q_{fit}$ was used according to the literature.[64] Here, Q_{gb}, $Q_{CT,C}$, $Q_{CT,A}$ and Q_{fit} are constant phase elements (CPE, Q), which are calculated via $Q = C^\alpha R^{\alpha-1}$, where C is the capacitance, R is the resistance and α is the fitting parameter.

We attribute the tiny shoulder in high frequency region (10^6–10^4 Hz) to the ionic transfer processes i.e., bulk (R_{bulk}) and grain boundary resistance of SSE particles (R_{gb}). The dominant semicircle in middle frequency region (10^3–10^0 Hz) resembles the charge transfer resistance of the cathode ($R_{CT,C}$) in parallel with SEI/Surface film capacitance ($Q_{CT,C}$). A wide semicircle and

Table 1. Name of the samples and their properties.

Samples	Coating	Coating dosage	Particle type
Pristine_mc	none	none	*multi*-crystalline
1LZO-NCM70_mc	Li_2ZrO_3	1 wt%	*multi*-crystalline
Pristine_sc	none	none	*single*-crystalline
1LZO-NCM70_sc	Li_2ZrO_3	1 wt%	*single*-crystalline

Batteries & Supercaps

Research Article
doi.org/10.1002/batt.202200100

Chemistry
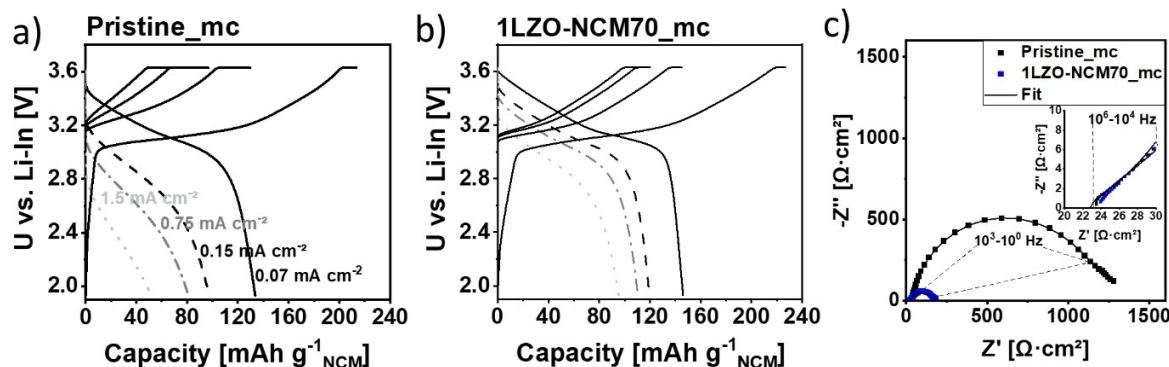Europe
European Chemical
Societies Publishing

Figure 7. Discharge rate performance of a) pristine∣SSE∣Li–In and b) 1LZO-NCM70∣SSE∣Li–In cells and c) their respective Nyquist plots. The impedance data were acquired at 3.63 V after initial charge. Both cells were cycled in the potential range of 3.63 to 1.93 V with the discharge current densities of 0.07, 0.15, 0.75, 1.5 mA cm^{-2} at 25 °C. The charging current was kept constant at 0.15 mA cm^{-2} and followed by a constant voltage step for each cycle.

sloping in low frequencies ($\leq 10^0$ Hz) correspond to the interface resistance at Li–In∣SSE ($R_{CT,A}$) and the bulk transfer processes such as Li$^+$ diffusion in the NCM70 particles, respectively. The deconvolution of anodic semicircle is rather complex due to its overlap with cathodic semicircle and presence at lower frequencies. Therefore, it was fitted based on fitting values given in literature.[35] In line with that, Nyquist diagrams were plotted (Figure 7c) and fitting results were given in the Table 2.

It is clear that cathodic resistance dominates the overall resistance of the cell. This originates from interdiffusion of

transition metals,[65] highly impeding SEI components[31] as bare NCM particles in contact with SSE are vulnerable such parasitic events at CEI. Notably, $R_{CT,C}$ diminishes more than 8-fold (1149→140 Ω cm^2) in case of LZO dry-coating, confirming the beneficial effect of the coating procedure. The cyclic performance of the both materials (Figure 8) approve again the superiority of 1 wt% LZO coated-NCM70 as it exhibits an average CE of ~99.99% and discharge capacity of ~88 mAh g$^{-1}_{NCM}$ after 50 cycles. In contrast, a wobbling CE profile with the average of ~99.85% and discharge capacity of ~52 mAh g$^{-1}_{NCM}$ are observable for uncoated NCM70.

Table 2. Resistance and capacitance values obtained using an equivalent circuit.

Samples	R [Ω cm^2]			
	R_b	R_{gb}	$R_{CT,C}$	$R_{CT,A}$
Pristine_mc	23.6	2.3	1149	27.5
1LZO-NCM70_sc	24.2	3.5	140	15.5

Electrochemical characterization of single-crystalline NCM70 particles dry-coated by LZONPs

As the nickel content in the NRLOs increases, parasitic phase transitions in the crystal structure, i.e., H2-H3 become more pronounced causing enormous anisotropic contraction/expansion of particles, especially when *mc*-NRLOs are overcharged (>4.2 V). This behavior leads to internal cracking and deteriorates the particle integrity of NRLOs.[66] This degradation mechanism plays even a more critical role in SSBs, in which physical contact between SSE and cathode particles must be well-maintained. Unlike liquid electrolytes, SSE cannot flow into cracks and preserves ionic conduction pathways. Consequently, SSBs degrade dramatically due to enhanced inner resistance in case of particle cracking and loss of particle-to-particle contact. On the other hand, *sc*-NRLO particles exhibit isotropic unit cell expansion[67] and can maintain their particle morphology without cracking during prolonged cycling,[68,69] which makes these NCM materials especially attractive for solid-state batteries.[70,71]

Therefore, we evaluated the described procedure also for *sc*-NCM70 particles to contribute the above-described advantages. We find out that the resulting coating layer is homogenous but discrete on planar NCM70 surface and has no influence on the crystal structure of *sc*-NCM70 (Figure S11).

Evaluating the discharge rate capability of uncoated (Pristine_sc) and 1 wt% LZO coated *sc*-NCM70 materials
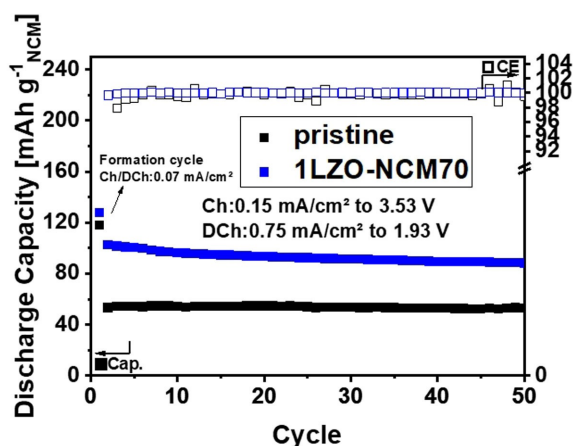

Figure 8. Cyclic performance pristine and dry-coated LZO NCM70. The cells were cycled in the potential range of 3.53 to 1.93 V with the discharge current density of 0.75 mA cm^{-2} at 25 °C. The charging current was kept constant at 0.15 mA cm^{-2} for each cycle.

Batteries & Supercaps

Research Article
doi.org/10.1002/batt.202200100

**Chemistry
Europe**
European Chemical
Societies Publishing

(1LZO-NCM70_sc); in the first cycle, both materials exhibit quite similar charge capacities ~233 mAh g$^{-1}_{NCM}$, whereas the discharge capacities differ from each other; 153 and 162 mAh g$^{-1}_{NCM}$ for Pristine_sc and 1LZO-NCM70_sc, respectively (Figure 9a and b). In addition to that, ICE improves from 65.2% to 69.8%, if the coating procedure is applied. Notably, the enhancement in the rate performance becomes distinctive looking at the highest discharge current density of 1.5 mA cm^{-2}, where the extracted capacities are 107 and 129 mAh g$^{-1}_{NCM}$ for Pristine_sc and 1LZO-NCM70_sc, respectively.

We accredit above advancement to two aspects, the suppression of CEI reactions and improved structural stability for NCM70 via the protective LZO layer. EIS Spectra (Figure 9c) approves the former as $R_{CT,C}$ drops down from 130 to 73 Ω cm^2, signifying reduced interface resistance. When the cells are charged >4.2 V vs. Li/Li$^+$ (overdelithiation of NCM70) (Figure 9d), a detrimental phase transition (H2-H3) occurs for both materials that can lead to formation of Li$^+$-impeding nickel oxides[72] as well as loss of physical contact between SSE and active material due to sudden contraction of Ni-Rich NCM70 particles.[73] This phase change is more pronounced and irreversible for Pristine_sc in comparison with 1LZO-NCM70_sc, confirming the latter.

The given CAMs are cycled for 50 cycles (Figure 10a) and the extracted capacity is found to be around 160 mAh g$^{-1}_{NCM}$ for both materials in the first cycle. This behavior is expected because the symmetrically-applied current was chosen to be significantly low (0.07 mA cm^2), in order to minimize kinetic limitations.

Moreover, in contrast to rate capability test (Figure 9a-b), no constant voltage step is applied during the charging. Therefore, the materials experience less stress, which hides the positive effect of the LZO coating at the first glance. However, following asymmetrical cycling with moderate current densities reveals the superiority of the coated material as Pristine_sc and 1LZO-NCM70 exhibit a capacity retention of 74.3% and 90.1% after 50 cycles, respectively. A stronger voltage decay (Ohmic drop) $\triangle V = 0.57$ V is noticeable for Pristine_sc at the beginning of the discharge step at the 50th cycle (Figure 10b), when comparing with the voltage loss of 1LZO-NCM70_sc $\triangle V = 0.27$ V. This result matches with the dQ/dV plots (Figure 10c) since the potential distance between the highest redox peaks is ~0.5 V for Pristine_sc at the 50th cycle, being more than 3-fold
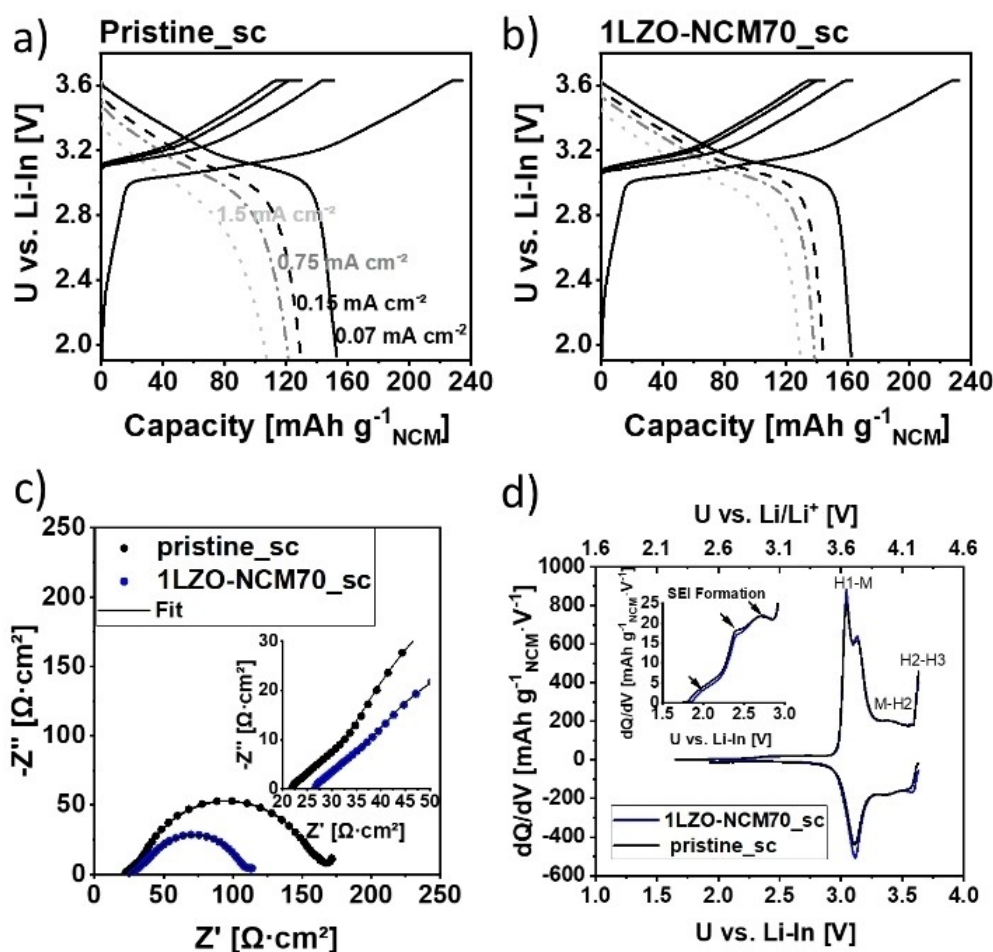

Figure 9. a) Cyclic performance for Pristine_sc (black) and 1LZO-NCM70_sc (blue) over 50 cycles and corresponding b) voltage and c) dQ/dV profiles at 1st and 50th cycles. The cells were cycled in the potential range of 3.53 to 1.93 V with the discharge current density of 0.75 mA cm^{-2} at 25°C. The charging current was kept constant at 0.15 mA cm^{-2} followed by a constant voltage step for each cycle.

Batteries & Supercaps

Research Article
doi.org/10.1002/batt.202200100

Chemistry
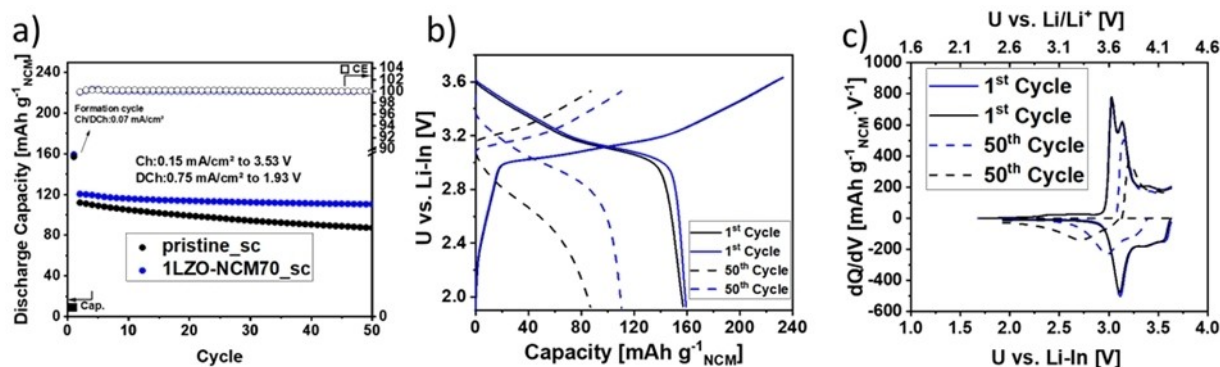Europe
European Chemical
Societies Publishing

Figure 10. Discharge rate performance of a) Pristine_sc|SSE|Li–In, b) 1LZO-NCM70_sc|SSE|Li–In cells, c) their respective Nyquist plots and d) dQ/dV plots at the first cycle. The impedance data were acquired at 3.63 V after initial charge. Both cells were cycled in the potential range of 3.63 to 1.93 V with the discharge current densities of 0.07, 0.15, 0.75, 1.5 mA cm^{-2} at 25 °C. The charging current was kept constant at 0.15 mA cm^{-2} for each cycle.
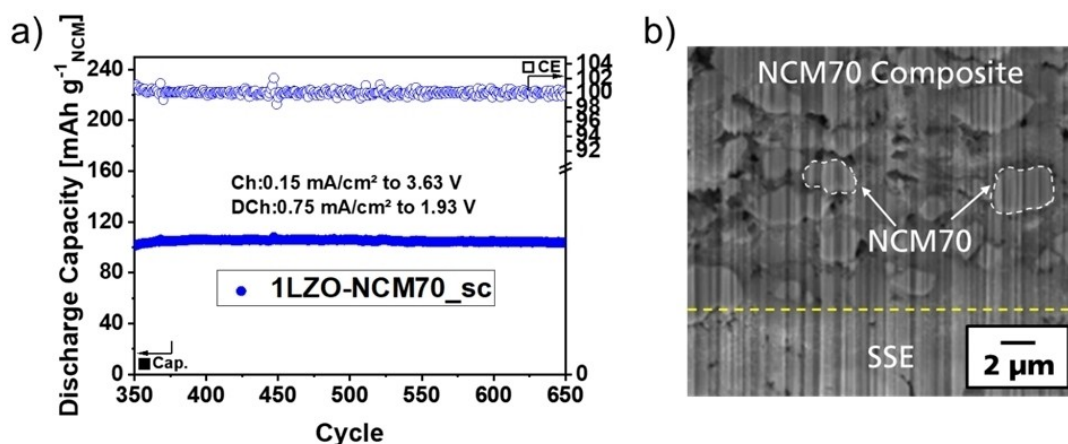

Figure 11. a) cyclic performance for 1LZO-NCM70_sc|SSE|Li–In cell and b) cross-sectional FIB SEM image of its cathode composite after 650 cycles, acquired at the tilt angle of 37.5° with the magnification of 2000×. The scaling was corrected with respect to the tilt angle and illustrated accordingly.

that of 1LZO-NCM70_sc (~0.16 V). This indicates enhanced polarization resistance of the pristine CAM as compared to 1LZO-NCM70_sc.

Considering that 1LZO-NCM70_sc is the best performing CAM out of others, it was strained up to 3.63 V for further 650 cycles (Figure 11a). The material exhibits a tremendous capacity retention of ~86.1 % and relatively minor interfacial resistance increment from 100th to 650th cycle (Figure S12). Cross-sectional post-mortem FIB-SEM images (Figure 11b) indicate well-maintained physical contact between SSE and 1LZO-NCM70_sc cathode composite layer even after 650 cycles. Also, no particle cracking or intergranular disintegration are observed for NCM70 particles after prolonged cycling, owing to their single crystallinity.

Conclusion

Herein, we demonstrate a versatile, facile and environmentally friendly dry-coating method, which is highly scalable (up to 500 kg per batch) and applicable for Ni-rich CAM via fumed oxide nanostructured particles. Amongst other coatings, parti-

ally amorphous lithium zirconate nanostructured particles, containing precursor phases (i.e., ZrO$_2$ and Li$_2$CO$_3$), provides high rate capability (1.5 mA cm^{-2}) and long-term stability for NCM70 (Capacity retention of 86.1 % at 650th cycle). The interfacial resistance reduces in NCM|SSE|Li–In half-cells in SSBs (130→73 Ω cm^2), when the coating dosage is optimized to 1 wt% during the high intensity mixing process. The obtained protective films are porous and stay firmly attached on the NCM surface regardless of particle structure (*single* or *multi-crystalline*), promising strong feasibility of the procedure. Unlike sol-gel coatings, a *post*-calcination step is not necessary, as high mechanical forces and strong van der Waals interactions between the host and high surface area of guest particles provide readily an intimate contact between CAM and the coating material. The presented work displays an effective way to create a buffer layer interlaying Ni-rich CAM (i.e., NCM70) and SSE (i.e., Li$_6$PS$_5$Cl) that is applicable to various particle morphologies and coating materials, being an important step in the direction of scalable component processing for high-energy solid-state batteries.

Experimental Section

Material preparation

The active materials NCM70 (Type PLB-H7) were purchased by Gelon Energy Corporation.

To synthesize the solid electrolyte powder, mechanical milling was carried out as instructed in the former works.[18] The resulting solid electrolyte powder is impurity-free Li_6PS_5Cl with argryrodite crystalline structure (Figure S1). It has an average particle size of 3–4 μm and exhibits an ionic conductivity of ~3 mS cm^{-1} (Figure S2).

For the anode material, lithium and indium foils (Li–In) were bought that have the thickness of 50 and 100 μm, respectively (Sigma Aldrich).

Synthesis of LZONPs

7.940 kg of a solution containing 2.725 kg of a commercial solution (Borchers® Deca Lithium2), containing 2 wt% lithium in the form of lithium neodecanoate and 2.984 kg of a commercial solution (Octa Solingen® Zirconium 12), containing 12 wt% Zr in the form of zirconium ethylhexanoate, and 2.231 kg 2-ethylhexanoic acid, were mixed, resulting in a clear solution. This solution represents the theoretical composition of Li_2ZrO_3.

An aerosol was formed of 2.5 kg h^{-1} stream of this solution and 15 Nm^3 h^{-1} stream of air via a two-component nozzle and sprayed into a tubular reaction with a burning flame. The burning gases of the flame consist of 4 Nm^3 h^{-1} hydrogen and 75 Nm^3 h^{-1} of air. Additionally, 25 Nm^3 h^{-1} secondary air was used. Leaving the reactor, the reaction gases were cooled down and filtered.

Dry-coating of LZONPs on NCM70

The NCM70 powder (GELON ENERGY CORP., Type PLB-H7) was mixed with the respective amount (1.0 wt%) of a fumed LZO powder (VP LZO, Evonik Operations GmbH) in a high intensity laboratory mixer (SOMAKON mixer MP-GL with 0.5 L mixing unit) at first for 1 min at 500 rpm to homogenize the two powders. Subsequently, the mixing intensity was increased to 2000 rpm for 5 min to achieve the dry-coating of the NCM70 particles by LZO. The mixing container contains eight blades, which are rotated by two high-speed rotors. (Figure S3).

Material characterization

To examine crystallinity of NCM70 powders and LZONPs, XRD (Cu Kα, 40 kV, 40 mA) diffractograms were measured via a D5005 diffractometer (Siemens, Germany) in locked-coupled mode using scan speed of 0.2 s step^{-1} (step size: 2θ:0.02°). Kapton tape (3 M) was used to prevent degradation due to contact with the air.

Triple-point Brunauer-Emmett-Teller (BET) measurement was conducted within the partial pressure region p/p_o of 0.05 to 0.3, in order to determine SSA of LZO nanostructured particles. Prior to analysis, the samples were degassed for 20 min under vacuum at 150 °C. The BET analysis was carried out in accordance with DIN/ISO 9277.

SEM imaging was performed for NCM particles by a scanning electron microscopy (SEM) JSM-6060 (JEOL, Japan) using 10 kV acceleration voltage and a working distance of 9 mm. HR-SEM images were acquired by use of SEM JSM-7600F (JEOL, Japan) using acceleration voltage of 1 kV. HR-TEM images of fumed coating nanostructured particles were recorded via a field emission high-resolution transmission electron microscope Jeol 2010F (JEOL, Japan) using acceleration voltage of 200 kV, after dispersing the particles in 50:50 v.% distilled water and isopropanol solution and following drying step at room temperature for 30 min.

Raman spectroscopy was carried out using a Raman microscope (micro-Raman Spectrometer, Renishaw inVia PLC) with an excitation laser wavelength of 514 nm and a 50× lens. The laser beam density at the sample was 0.44 mW μm^{-2} and the acquisition time was 5×60 s. Particle size distribution of coating particles was analyzed by a laser particle size analyzer (LA-950, Horiba, Germany) after dispersing in distilled water containing Dolapix CE64 (dispersant agent) and following ultrasonication for 5 min.

Electrode and test-cell preparation

To prepare composite cathode powders, CAM (NCM70), conductive carbon additive vapor-grown carbon nanofibers (VG-CNF), and SSE (Li_6PS_5Cl) were consecutively mixed in the respective mass ratio of 60:35:5 for 30 min in an agate mortar.

The test cell was prepared using a die with a diameter of 13 mm as described elsewhere.[42] The cell has a stainless-steel outer housing with a Teflon liner (Figure S4). For a typical test cell, 150 mg (~750 μm) of the SSE powder (Li_6PS_5Cl) were evenly distributed inside the die with help of a micro-spatula. Afterwards, the SSE powder was once temporally compacted into pellet under approx. 25 MPa. Subsequently, 15 mg of cathode composite powder was homogeneously spread over the smooth surface of SSE pellet in the die and the cathode layer was temporarily compressed. On the other side of the cell stack, a lithium-indium alloy anode was laid down and pressed as described.[74] The cell stack was again compressed together with all components and completely pelletized under 300 MPa for 30 s by using a hydraulic press.

After pelletization, the cell stack was positioned inside the outer steel housing, where a screw sustains the electric contact in the cell. Then, the screw was fixed at 3.0 Nm (25 MPa) by means of a preset torque. All above-mentioned steps were conducted in an Ar filled glove box (<0.1 ppm H_2O and O_2).

Electrochemical testing procedures

Electrochemical impedance (EIS) was performed for half-cells using a VSP-300 (Bio-Logic, France) controlled by a computer. The test cell was charged to 3.63 V with a current density of 0.15 mA cm^{-2}. A constant voltage step (CVS) was thereafter applied until the current reached 0.01 mA to equilibrate the given potential. Afterwards, EIS was carried out with amplitude of 10 mV in a frequency range of 0.1 Hz–1 MHz at 25 °C under ambient pressure. The EIS results were analyzed using EC-Lab software.

For the rate performance test, the discharge currents were varied from 0.07 to 1.5 mA cm^{-2} at the constant charging rate of 0.15 mA cm^{-2} including a CVS. The cycling test, after the initial formation cycle at 3.63–1.93 V with a constant current of 0.07 mA cm^{-2}, was performed in the voltage range of 3.53–1.93 V with a current rate of 0.15 and 0.75 mA cm^{-2} for charge and discharge, respectively. Both tests were performed by a battery tester CTS-Lab (BaSyTec, Germany).

Acknowledgements

Conflict of Interest

The authors declare no conflict of interest.

Data Availability Statement

Research data are not shared.

[1] J. Betz, G. Bieker, P. Meister, T. Placke, M. Winter, R. Schmuch, *Adv. Energy Mater.* **2019**, *9*, 1803170.

[2] J. Janek, W. G. Zeier, *Nat Energy* **2016**, *1*, 16141.

[3] Y. Horowitz, C. Schmidt, D. Yoon, L. M. Riegger, L. Katzenmeier, G. M. Bosch, M. Noked, Y. Ein-Eli, J. Janek, W. G. Zeier, C. E. Diesendruck, D. Golodnitsky, *Energy Technol.* **2020**, *8*, 2000580.

[4] D. H. S. Tan, A. Banerjee, Z. Chen, Y. S. Meng, *Nat. Nanotechnol.* **2020**, *15*, 170.

[5] A. Kwade, W. Haselrieder, R. Leithoff, A. Modlinger, F. Dietrich, K. Droeder, *Nat. Energy* **2018**, *3*, 290.

[6] S. Chae, M. Ko, K. Kim, K. Ahn, J. Cho, *Joule* **2017**, *1*, 47.

[7] F. Han, J. Yue, X. Zhu, C. Wang, *Adv. Energy Mater.* **2018**, *8*, 1703644.

[8] X. Han, Y. Gong, K. K. Fu, X. He, G. T. Hitz, J. Dai, A. Pearse, B. Liu, H. Wang, G. Rubloff, Y. Mo, V. Thangadurai, E. D. Wachsman, L. Hu, *Nat. Mater.* **2017**, *16*, 572.

[9] H. Xu, Y. Li, A. Zhou, N. Wu, S. Xin, Z. Li, J. B. Goodenough, *Nano Lett.* **2018**, *18*, 7414.

[10] J.-M. Doux, H. Nguyen, D. H. S. Tan, A. Banerjee, X. Wang, E. A. Wu, C. Jo, H. Yang, Y. S. Meng, *Adv. Energy Mater.* **2020**, *10*, 1903253

[11] S. Cangaz, F. Hippauf, F. S. Reuter, S. Doerfler, T. Abendroth, H. Althues, S. Kaskel, *Adv. Energy Mater.* **2020**, *3*, 2001320.

[12] R. Miyazaki, N. Ohta, T. Ohnishi, I. Sakaguchi, K. Takada, *J. Power Sources* **2014**, *272*, 541.

[13] J. Sakabe, N. Ohta, T. Ohnishi, K. Mitsuishi, K. Takada, *Commun. Chem.* **2018**, *1*, 13.

[14] D. H. S. Tan, Y.-T. Chen, H. Yang, W. Bao, B. Sreenarayanan, J.-M. Doux, W. Li, B. Lu, S.-Y. Ham, B. Sayahpour, J. Scharf, E. A. Wu, G. Deysher, H. E. Han, H. J. Hah, H. Jeong, J. B. Lee, Z. Chen, Y. S. Meng, *Science* **2021**, *373*, 1494.

[15] Y.-G. Lee, S. Fujiki, C. Jung, N. Suzuki, N. Yashiro, R. Omoda, D.-S. Ko, T. Shiratsuchi, T. Sugimoto, S. Ryu, J. H. Ku, T. Watanabe, Y. Park, Y. Aihara, D. Im, I. T. Han, *Nat. Energy* **2020**, *5*, 299.

[16] B. J. Neudecker, N. J. Dudney, J. B. Bates, *J. Electrochem. Soc.* **2000**, *147*, 517.

[17] Y. Amiki, F. Sagane, K. Yamamoto, T. Hirayama, M. Sudoh, M. Motoyama, Y. Iriyama, *J. Power Sources* **2013**, *241*, 583.

[18] F. Hippauf, B. Schumm, S. Doerfler, H. Althues, S. Fujiki, T. Shiratsuchi, T. Tsujimura, Y. Aihara, S. Kaskel, *Energy Storage Mater.* **2019**, *21*, 390.

[19] H. Liang, Z. Wang, H. Guo, J. Wang, J. Leng, *Appl. Surf. Sci.* **2017**, *423*, 1045.

[20] F. Strauss, T. Bartsch, L. de Biasi, A.-Y. Kim, J. Janek, P. Hartmann, T. Brezesinski, *ACS Energy Lett.* **2018**, *3*, 992.

[21] Y. Zhu, X. He, Y. Mo, *ACS Appl. Mater. Interfaces* **2015**, *7*, 23685.

[22] J. W. Fergus, *J. Power Sources* **2010**, *195*, 4554.

[23] M. Park, X. Zhang, M. Chung, G. B. Less, A. M. Sastry, *J. Power Sources* **2010**, *195*, 7904.

[24] S. Chida, A. Miura, N. C. Rosero-Navarro, M. Higuchi, N. H. Phuc, H. Muto, A. Matsuda, K. Tadanaga, *Ceram. Int.* **2018**, *44*, 742.

[25] S. Teragawa, K. Aso, K. Tadanaga, A. Hayashi, M. Tatsumisago, *J. Mater. Chem. A* **2014**, *2*, 5095.

[26] Z. Zhang, L. Zhang, Y. Liu, C. Yu, X. Yan, B. Xu, L. Wang, *J. Alloys Compd.* **2018**, *747*, 227.

[27] Q. Zhang, D. Cao, Y. Ma, A. Natan, P. Aurora, H. Zhu, *Adv. Mater.* **2019**, *31*, e1901131.

[28] L. E. Camacho-Forero, P. B. Balbuena, *J. Power Sources* **2018**, *396*, 782.

[29] S. Chen, D. Xie, G. Liu, J. P. Mwizerwa, Q. Zhang, Y. Zhao, X. Xu, X. Yao, *Energy Storage Mater.* **2018**, *14*, 58.

[30] D. Y. Oh, Y. J. Nam, K. H. Park, S. H. Jung, K. T. Kim, A. R. Ha, Y. S. Jung, *Adv. Energy Mater.* **2019**, *9*, 1802927.

[31] J. Auvergniot, A. Cassel, J.-B. Ledeuil, V. Viallet, V. Seznec, R. Dedryvère, *Chem. Mater.* **2017**, *29*, 3883.

[32] C. Yu, S. Ganapathy, E. R. H. van Eck, H. Wang, S. Basak, Z. Li, M. Wagemaker, *Nat. Commun.* **2017**, *8*, 1086.

[33] R. Koerver, I. Aygün, T. Leichtweiß, C. Dietrich, W. Zhang, J. O. Binder, P. Hartmann, W. G. Zeier, J. Janek, *Chem. Mater.* **2017**, *29*, 5574.

[34] R. Koerver, W. Zhang, L. de Biasi, S. Schweidler, A. O. Kondrakov, S. Kolling, T. Brezesinski, P. Hartmann, W. G. Zeier, J. Janek, *Energy Environ. Sci.* **2018**, *11*, 2142.

[35] W. Zhang, D. A. Weber, H. Weigand, T. Arlt, I. Manke, D. Schröder, R. Koerver, T. Leichtweiss, P. Hartmann, W. G. Zeier, J. Janek, *ACS Appl. Mater. Interfaces* **2017**, *9*, 17835.

[36] C. Zheng, L. Li, K. Wang, C. Wang, J. Zhang, Y. Xia, H. Huang, C. Liang, Y. Gan, X. He, X. Tao, W. Zhang, *Batteries & Supercaps* **2021**, *4*, 8.

[37] K. Meng, Z. Wang, H. Guo, X. Li, D. Wang, *Electrochim. Acta* **2016**, *211*, 822.

[38] Z. Wang, S. Huang, B. Chen, H. Wu, Y. Zhang, *J. Mater. Chem. A* **2014**, *2*, 19983.

[39] R. S. Negi, P. Minnmann, R. Pan, S. Ahmed, M. J. Herzog, K. Volz, R. Takata, F. Schmidt, J. Janek, M. T. Elm, *Chem. Mater.* **2021**, *33*, 6713.

[40] Y.-J. Kim, R. Rajagopal, S. Kang, K.-S. Ryu, *Chem. Eng. J.* **2020**, *386*, 123975.

[41] X. Li, L. Jin, D. Song, H. Zhang, X. Shi, Z. Wang, L. Zhang, L. Zhu, *J. Energy Chem.* **2020**, *40*, 39.

[42] S. Ito, S. Fujiki, T. Yamada, Y. Aihara, Y. Park, T. Y. Kim, S.-W. Baek, J.-M. Lee, S. Doo, N. Machida, *J. Power Sources* **2014**, *248*, 943.

[43] U. Ulissi, M. Agostini, S. Ito, Y. Aihara, J. Hassoun, *Solid State Ionics* **2016**, *296*, 13.

[44] K. Okada, N. Machida, M. Naito, T. Shigematsu, S. Ito, S. Fujiki, M. Nakano, Y. Aihara, *Solid State Ionics* **2014**, *255*, 120.

[45] X. Miao, H. Ni, H. Zhang, C. Wang, J. Fang, G. Yang, *J. Power Sources* **2014**, *264*, 147.

[46] Y. Wu, M. Li, W. Wahyudi, G. Sheng, X. Miao, T. D. Anthopoulos, K.-W. Huang, Y. Li, Z. Lai, *ACS Omega* **2019**, *4*, 13972.

[47] H. Zhang, J. Xu, J. Zhang, *Front. Mater.* **2019**, *6*, 206.

[48] W. Lee, Y. Park, *J. Electrochem. Sci. Technol.* **2018**, *9*, 176.

[49] J. Zhang, H. Zhang, R. Gao, Z. Li, Z. Hu, X. Liu, *Phys. Chem. Chem. Phys.* **2016**, *18*, 13322.

[50] M. J. Herzog, N. Gauquelin, D. Esken, J. Verbeeck, J. Janek, *Energy Technol.* **2021**, *9*, 2100028.

[51] E. A. Wu, C. Jo, D. H. S. Tan, M. Zhang, J.-M. Doux, Y.-T. Chen, G. Deysher, Y. S. Meng, *J. Electrochem. Soc.* **2020**, *167*, 130516.

[52] B. Song, W. Li, S.-M. Oh, A. Manthiram, *ACS Appl. Mater. Interfaces* **2017**, *9*, 9718.

[53] P. Albers, M. Maier, M. Reisinger, B. Hannebauer, R. Weinand, *Cryst. Res. Technol.* **2015**, *50*, 846.

[54] M. Y. Ali, H. Orthner, H. Wiggers, *Materials (Basel)* **2021**, *14*.

[55] L. Zhang, T. Dong, X. Yu, Y. Dong, Z. Zhao, H. Li, *Mater. Res. Bull.* **2012**, *47*, 3269.

[56] Y. Xiao, L. J. Miara, Y. Wang, G. Ceder, *Joule* **2019**, *3*, 1252.

[57] G. Lefebvre, L. Galet, A. Chamayou, *Powder Technol.* **2011**, *208*, 372.

[58] R. Sharma, G. Setia, *Powder Technol.* **2019**, *356*, 458.

[59] J. Zhang, C. Zheng, L. Li, Y. Xia, H. Huang, Y. Gan, C. Liang, X. He, X. Tao, W. Zhang, *Adv. Energy Mater.* **2020**, *10*, 1903311.

[60] F. Walther, F. Strauss, X. Wu, B. Mogwitz, J. Hertle, J. Sann, M. Rohnke, T. Brezesinski, J. Janek, *Chem. Mater.* **2021**, *33*, 2110.

[61] S. H. Jung, K. Oh, Y. J. Nam, D. Y. Oh, P. Brüner, K. Kang, Y. S. Jung, *Chem. Mater.* **2018**, *30*, 8190.

[62] A.-Y. Kim, F. Strauss, T. Bartsch, J. H. Teo, T. Hatsukade, A. Mazilkin, J. Janek, P. Hartmann, T. Brezesinski, *Chem. Mater.* **2019**, *31*, 9664.

[63] F. Walther, F. Strauss, X. Wu, B. Mogwitz, J. Hertle, J. Sann, M. Rohnke, T. Brezesinski, J. Janek, *Chem. Mater.* **2021**, *33*, 2110.

[64] P. Vadhva, J. Hu, R. Stocker, M. Braglia, D. J. L. Brett, R. J. E. Alexander, *ChemElectroChem* **2021**, doi.org/10.1002/celc.202100108.

[65] A. Sakuda, A. Hayashi, M. Tatsumisago, *Chem. Mater.* **2010**, *22*, 949.

[66] X. Chen, Y. Tang, C. Fan, S. Han, *Electrochim. Acta* **2020**, *341*, 136075.

[67] Y. Liu, J. Harlow, J. Dahn, *J. Electrochem. Soc.* **2020**, *167*, 20512.

[68] X. Fan, G. Hu, B. Zhang, X. Ou, J. Zhang, W. Zhao, H. Jia, L. Zou, P. Li, Y. Yang, *Nano Energy* **2020**, *70*, 104450.

[69] J. E. Harlow, X. Ma, J. Li, E. Logan, Y. Liu, N. Zhang, L. Ma, S. L. Glazier, M. M. E. Cormier, M. Genovese, S. Buteau, A. Cameron, J. E. Stark, J. R. Dahn, *J. Electrochem. Soc.* **2019**, *166*, A3031-A3044.

[70] C. Doerrer, I. Capone, S. Narayanan, J. Liu, C. R. M. Grovenor, M. Pasta, P. S. Grant, *ACS Appl. Mater. Interfaces* **2021**, *13*, 37809.

[71] X. Li, W. Peng, R. Tian, D. Song, Z. Wang, H. Zhang, L. Zhu, L. Zhang, *Electrochim. Acta* **2020**, *363*, 137185.

[72] J. Yang, Y. Xia, *ACS Appl. Mater. Interfaces* **2016**, *8*, 1297.

[73] H.-H. Ryu, B. Namkoong, J.-H. Kim, I. Belharouak, C. S. Yoon, Y.-K. Sun, *ACS Energy Lett.* **2021**, *6*, 2726.

[74] K. Takada, *Solid State Ionics* **1996**, *86–88*, 877.